

Investigation of γ softness: Lifetime measurements in $^{104,106}\text{Ru}$

Esmaylzadeh, A.; Blazhev, A.; Nomura, Kosuke; Jolie, J.; Beckers, M.; Fransen, C.; Gerst, R.-B.; Harter, A.; Karayonchev, V.; Knafla, L.; ...

Source / Izvornik: **Physical Review C, 2022, 106**

Journal article, Published version

Rad u časopisu, Objavljena verzija rada (izdavačev PDF)

<https://doi.org/10.1103/PhysRevC.106.064323>

Permanent link / Trajna poveznica: <https://urn.nsk.hr/urn:nbn:hr:217:661582>

Rights / Prava: [In copyright](#)/[Zaštićeno autorskim pravom.](#)







Download date / Datum preuzimanja: **2024-09-11**



Repository / Repozitorij:

[Repository of the Faculty of Science - University of Zagreb](#)



Investigation of γ softness: Lifetime measurements in $^{104,106}\text{Ru}$ A. Esmaylzadeh ^{1,*}, A. Blazhev,¹ K. Nomura ², J. Jolie,¹ M. Beckers,¹ C. Fransen ¹, R.-B. Gerst,¹ A. Harter ¹, V. Karayonchev,^{1,3} L. Knaffla ¹, M. Ley,¹ and F. von Spee ¹¹Universität zu Köln, Institut für Kernphysik, D-50937 Köln, Germany²Department of Physics, Faculty of Science, University of Zagreb, 10000 Zagreb, Croatia³TRIUMF, 4004 Wesbrook Mall, Vancouver, BC V6T 2A3, Canada

(Received 7 July 2022; revised 26 October 2022; accepted 8 December 2022; published 21 December 2022)

Lifetimes of the 2_1^+ , 4_1^+ , 6_1^+ , 2_γ^+ , and 3_γ^+ states in $^{104,106}\text{Ru}$ were measured by using the recoil-distance Doppler-shift technique and the Cologne Plunger device. Low-lying excited states in both nuclei were populated in a $^{104}\text{Ru}(^{18}\text{O}, ^{18}\text{O})^{104}\text{Ru}^*$ inelastic scattering and in a $^{104}\text{Ru}(^{18}\text{O}, ^{16}\text{O})^{106}\text{Ru}$ two-neutron transfer reaction using the Cologne FN Tandem accelerator. The experimental energy levels and deduced electromagnetic transition probabilities are compared in the context of γ softness and the mapped interacting boson model with input from the microscopic self-consistent mean-field calculation using a Gogny interaction. The newly obtained results for the γ band give a more detailed insight about the triaxial behavior of $^{104,106}\text{Ru}$. The results will be discussed in the context of γ soft and rigid triaxial behavior which is present in the neutron-rich Ru isotopes.

DOI: [10.1103/PhysRevC.106.064323](https://doi.org/10.1103/PhysRevC.106.064323)

I. INTRODUCTION

The ruthenium ($Z = 44$) and palladium ($Z = 46$) isotopes are located between the strontium ($Z = 38$), zirconium ($Z = 40$), and molybdenum ($Z = 42$) isotopes, which undergo a transition from spherical to a strongly deformed type of structure [1–6], and the less deformed cadmium (Cd , $Z = 48$) and tin (Sn , $Z = 50$) isotopes [7,8]. In the neutron-rich region around $Z \approx 40$ and $N \approx 60$, the transition from a spherical to a deformed type of structure of the ground-state band accompanied by shape coexistence is expected to happen by going from 58 to 60 neutrons. Compared with the related Sr and Zr isotopes, no shape coexistence is observed for $^{102,104}\text{Ru}_{60}$ and the transition is more gradual. However, some studies of static and dynamic quadrupole moments indicate that the shape coexistence might still persist in this nucleus [2,9,10].

Different experiments show that the isotopic chains of molybdenum, ruthenium, and palladium possess signatures indicating γ -soft behavior [11–16,18]. In even-even nuclei the 2_1^+ state is related to the quadrupole deformation and the γ band is sensitive to the triaxial motion of the nucleus. A triaxial nucleus rotates around all three axes of the intrinsic body and has its potential-energy surface minimum at $\gamma = 30^\circ$. Two models discussing the triaxial shape are the Wilets-Jean γ -soft rotor model [17] and the Davydov-Filippov rigid triaxial rotor model [18–20]. In the γ -soft model the potential-energy surface is independent of γ and shows a broad minimum in the γ degree of freedom, while the rigid-rotor model has a distinct minimum at $\gamma = 30^\circ$. A useful tool to distinguish between these two limits of a triaxial

nucleus is the staggering parameter, which is defined as [21]

$$S(J) = \frac{[E(J) - 2E(J-1) + E(J-2)]}{E(2_1^+)}, \quad (1)$$

where $E(J)$ represents the energy levels of the γ band with the corresponding spin J . The staggering parameter describes the clustering and spacing of states in the γ band where a positive value for odd-spin levels and negative value for even-spin levels corresponds to a γ -soft case and the opposite values for a γ -rigid nucleus. In Fig. 1 the staggering parameters for the Ru isotopes with neutron numbers from 56 to 68 ($^{100-112}\text{Ru}$) are shown, calculated for spin $J = 4, 5, 6, 7$ states of the γ band. According to the available data for ^{100}Ru , a γ -soft structure is expected. For the Ru isotopes with 58 to 64 neutrons ($^{102-108}\text{Ru}$) a less pronounced even-odd spin staggering is observed, which might be an indicator of a less pronounced softness in these nuclei. ^{110}Ru seems to be a transitional nucleus from a γ -soft behavior occurring in the lighter Ru isotopes to a rather more γ -rigid behavior in ^{112}Ru . The molybdenum and palladium isotones of $^{104,106}\text{Ru}$, i.e., $^{102,104}\text{Mo}$, and $^{106,108}\text{Pd}$ also show signs of γ softness in terms of staggering parameter and $R_{4/2}$ ratio [23–26,29]. However, the signs are only weakly pronounced for ^{104}Mo and the neutron-rich molybdenum isotopes [29,30].

Further signatures to characterize the shape and behavior of a nucleus are the $R_{4/2} = E(4_1^+)/E(2_1^+)$ and $B_{4/2} = B(E2; 4_1^+ \rightarrow 2_1^+)/B(E2; 2_1^+ \rightarrow 0_1^+)$ ratios. The $R_{4/2}$ ratio for the ruthenium isotopes increases from around 2.1 for ^{98}Ru up to a maximum of 2.8 for ^{110}Ru , which is also the midshell nucleus with $N = 66$. Afterwards the ratio decreases slowly down to 2.6 for ^{116}Ru . The $R_{4/2}$ ratios of $^{104,106}\text{Ru}$, discussed in this work, are 2.48(1) and 2.65(1), respectively. These values are close to the γ -soft limit which is at 2.5. The $B_{4/2}$

* aesmaylzadeh@ikp.uni-koeln.de

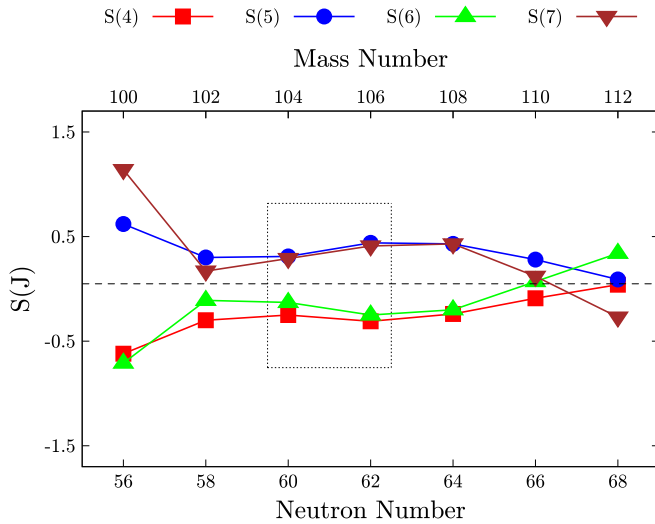


FIG. 1. (a) The staggering parameter $S(J)$ for the $^{100-112}\text{Ru}$ isotopes calculated using Eq. (1). The energy levels are taken from the Nuclear Data Sheets [22–28].

ratio for ^{98}Ru is 1.9(5) and thus nearly the spherical limit [31]. The $^{100,102,104}\text{Ru}$ isotopes show a $B_{4/2}$ ratio of ≈ 1.5 which is closer to the rotational limit [22–24]. The lifetime of the 4_1^+ state in ^{106}Ru was not available in the past, but will be determined in the course of this work. For the neutron-rich isotopes $^{108,110}\text{Ru}$, the ratios are 1.7(5) and 1.3(5), respectively [26,27]. The lifetime information about the 4_1^+ state in ^{106}Ru is important to close the gap between the stable and neutron-rich Ru isotopes, i.e., between $^{100-104}\text{Ru}$ and $^{108-112}\text{Ru}$.

II. EXPERIMENT

To populate low-lying states in ^{104}Ru and ^{106}Ru , the inelastic-scattering reaction $^{104}\text{Ru}(^{18}\text{O}, ^{18}\text{O}')^{104}\text{Ru}^*$ and the two-neutron transfer reaction $^{104}\text{Ru}(^{18}\text{O}, ^{16}\text{O})^{106}\text{Ru}$ were used. The enriched ^{104}Ru target had a thickness of 0.15 mg/cm² that was evaporated onto a natural vanadium 0.78 mg/cm² backing. The target was stretched in parallel to a natural vanadium stopper foil with a thickness of 3.1 mg/cm² inside the Cologne Plunger device [32]. Still traces of ^{102}Ru were observed in the reaction. The ^{18}O beam impinged on the target with a beam current of ≈ 1 pA using an energy of 57 MeV provided by the Cologne 10 MV FN-Tandem accelerator. The stopper foil acts as a stopper for the ejectiles produced in the reaction, i.e., recoiling $^{104,106}\text{Ru}$ nuclei. The Cologne Plunger device was used in conjunction with eleven high-purity germanium (HPGe) detectors forming two rings (backward and forward) around the target chamber to detect γ rays [32]. The six backward and five forward detectors were placed at angles of 45° and 142° with respect to the beam direction. As in previous experiments [15,16,33,34], six solar cells (PIN diodes) were installed at backward angles to detect the backscattered beam-like light recoiling fragments and to limit the kinematics of the recoiling reaction products. Ten target-to-stopper distances (44, 53, 63, 93, 143, 343, 843, 1543, 2843, and 3743 μm) with respect to the electrical contact of the foils were measured in seven days

of beam time to achieve sufficient coverage and statistics to apply the recoil distance Doppler-shift (RDDS) technique and the differential decay curve method (DDCM) [32,35]. To determine the absolute distance, the capacitance method described in Refs. [32,36] was used. In addition, an optical distance measurement device was used to obtain the absolute distances [37]. Both methods yield consistent results for the so-called zero distances of 43(5) μm where the uncertainty is used as an error for each absolute distance. The zero distance is defined as the minimal distance between target and stopper foil, where no electrical contact occurs. To determine the velocity of the recoiling nuclei, the Doppler shift of the most intense transitions are used. The resulting recoil velocity amounts to $v/c = 2.10(6)\%$ and $v/c = 2.01(10)\%$ for ^{104}Ru and ^{106}Ru , respectively. The red rectangle in Fig. 2(a) indicates the asymmetric gate that has been applied to select the backscattered $^{16,18}\text{O}$ particle to observe the coincident γ rays of the corresponding reaction partner (either ^{104}Ru or ^{106}Ru). An asymmetric gate has been applied to avoid a possible contamination of the α -transfer channel which results in ^{108}Pd , which is marked with a blue rectangle in Fig. 2(a). A distinction of the inelastic-scattering channels (^{102}Ru and ^{104}Ru) and the two neutron transfer channel (^{106}Ru) with the applied particle gate was not possible due to the energy and angular straggling of the recoiling ^{16}O and ^{18}O particles as well as the angular coverage of the solar cells. In Figs. 2(b) and 2(c), the γ -ray spectrum summing up all distances is shown for the energy range from 170 keV up to 1750 keV. In Figs. 3(b) and 3(c) the partial level scheme is shown which was built using the information of corresponding γ -ray spectrum, where the spins and parities are taken from the literature [24,25]. The states populated in this experiment are consistent with previous inelastic-scattering and two-neutron transfer experiments [10,25,38–41]. The arrow width in the partial level scheme describes the intensity of the observed transition that are summarized in Table I. The observation limit is about 0.2% and 2% relative to the $2_1^+ \rightarrow 0_1^+$ transitions of ^{104}Ru and ^{106}Ru , respectively. The large difference in the observation limit results from the approximately ten-times higher cross section for the inelastic scattering compared with the two-neutron transfer reaction. This leads to more statistics and hence a more sensitive observation limit. The strongest γ rays in coincidence to the particle gate onto $^{16,18}\text{O}$ belong to ^{102}Ru marked with *, ^{104}Ru and ^{106}Ru , where the γ rays are labeled with the corresponding transition between the two involved state, as can be seen in Figs. 2(b) and 2(c).

III. ANALYSIS

The lifetimes of the 2_1^+ , 4_1^+ , 6_1^+ , 2_γ^+ , and 3_γ^+ states in both nuclei were analyzed using the Bateman equations [42] and the well-established differential decay curve method (DDCM) [32,35]. The DDCM has specific advantages such as the minimization of systematic errors, the usage of directly derived experimental values and relative distances and the fact that no assumptions about the shape of the decay curve $R(t)$ are required. To determine lifetimes using the DDCM, the

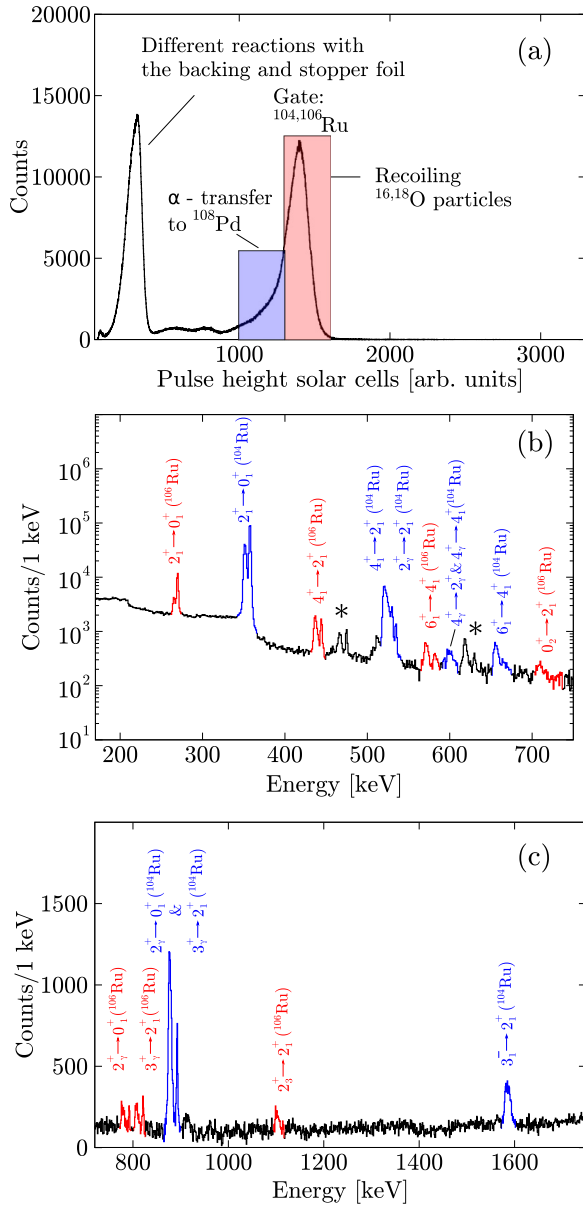


FIG. 2. (a) The summed solar cell spectrum of all distances. The red rectangle shows the applied gate to select the recoiling $^{16,18}\text{O}$ particles to obtain a γ spectrum of $^{104,106}\text{Ru}$. The gate on $^{16,18}\text{O}$ has been applied asymmetric to avoid a possible contamination of the α -transfer channel. (b), (c) The summed γ -ray spectrum for all distances after applying a particle gate which is indicated by the red rectangle in panel (a) for the energy range is from 170 up to 750 keV and 720 up to 1750 keV, respectively. The observed transitions of ^{104}Ru are marked in blue and for ^{106}Ru in red. The transitions marked with “*” belong to the inelastic scattering of ^{102}Ru , which are the $2_1^+ \rightarrow 0_1^+$ and $4_1^+ \rightarrow 2_1^+$ transitions. Note that the y scale is logarithmic in panel (b) and a linear scale is used in panel (c).

program NAPATAU [43] was used. A detailed description of both methods is given in Ref. [32]. Due to a lack of statistics in γ - γ coincidences, only particle-gated single γ -ray spectra were used to determine the lifetimes. For some low populated

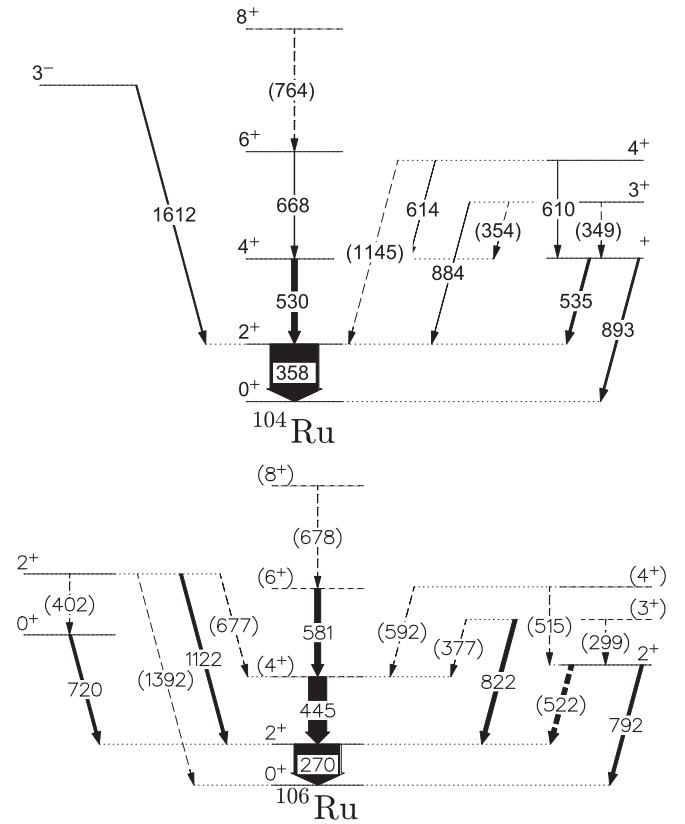


FIG. 3. Partial level scheme of the observed states in ^{104}Ru and ^{106}Ru populated in the inelastic scattering or in the two-neutron transfer reaction. The width of the transition arrows corresponds to the observed intensities (see Table I) and the dashed lines indicate known transitions not observed in this experiment.

states the method explained and applied in Refs. [15,16,44] was used to determine the lifetimes. Therefore, the summed spectra of all distances j was solved with the following equation:

$$R_{\text{sum}} = \frac{\sum_j I_j^u}{\sum_j I_j^u + \sum_j I_j^s} = \sum_j n_j R(t_j), \quad (2)$$

with I_j^u and I_j^s being the intensities of the unshifted and shifted components, respectively. The normalization factor n_j has been obtained by applying a gate for each distance on the $2_1^+ \rightarrow 0_1^+$ transition of ^{104}Ru and ^{106}Ru corresponding to 270.1 and 358.0 keV, respectively, and integrating the resulting particle spectrum. The time of flight for each distance is described by t_j and $R(t_j)$ is the decay curve described by the Bateman equations [42]. The lifetime τ is the only free parameter in solving this equation [15,16,44,45].

Here, a top-to-bottom approach was used to adjust the feeding pattern influencing the lifetimes of lower-lying states. For the cases of higher-lying states and of low statistics, Eq. (2) has been used to derive lifetimes. This is realized by applying a Monte Carlo approach with 10^7 iterations and which varies n_j , R_{sum} , v/c and the distance within the uncertainties. From the resulting distribution, the lifetimes and

TABLE I. Relative transition intensities observed in the inelastic scattering $^{104}\text{Ru}(^{18}\text{O}, ^{18}\text{O}')^{104}\text{Ru}^*$ and the two-neutron transfer $^{104}\text{Ru}(^{18}\text{O}, ^{16}\text{O})^{106}\text{Ru}$ reaction. The intensities were normalized to the $2_1^+ \rightarrow 0_1^+$ transition of the respective nucleus and the energies are taken from Refs. [24,25].

Transition	^{104}Ru		^{106}Ru	
	Transition energy [keV]	Intensity	Transition energy [keV]	Intensity
$2_1^+ \rightarrow 0_1^+$	358.0(1)	100.0(22)	270.1(1)	100.0(35)
$4_1^+ \rightarrow 2_1^+$	530.5(1)	11.4(32)	444.6(2)	41.1(17)
$6_1^+ \rightarrow 4_1^+$	667.9(3)	1.1(1)	581.1(2)	11.8(8)
$2_\gamma^+ \rightarrow 2_1^+$	535.1(1)	5.5(2)	522.2(1)	
$2_\gamma^+ \rightarrow 0_1^+$	893.1(1)	4.3(2)	792.3(1)	7.4(8)
$3_\gamma^+ \rightarrow 2_1^+$	884.4(1)	0.7(2)	821.5(1)	11.8(9)
$4_\gamma^+ \rightarrow 2_\gamma^+$	609.5(1)	0.4(1)	515	
$4_\gamma^+ \rightarrow 4_1^+$	614.2(1)	0.2(1)	592	
$2_3^+ \rightarrow 2_1^+$	1157.4(1)		1122.2(1)	8.1(9)
$3_1^- \rightarrow 2_1^+$	1612.4(1)	2.7(2)		
$0_2^- \rightarrow 2_1^+$	630.3(3)		720.5(1)	5.2(8)

the corresponding uncertainty is derived as mean and standard deviation.

For the determination of the lifetimes of states with higher statistics of the decay transition, the Bateman equations were solved. Here, a Monte Carlo approach was also used which varies all parameters like absolute distance, $R(t)$, v/c , and possible feeding contributions like feeding intensity and feeding lifetime within their respective uncertainties. The adopted values and their corresponding errors are calculated by using a Monte Carlo simulation. To account for nonstatistical sources of uncertainty, a 5% systematic error is added to the adopted value. Potential systematic uncertainties are caused by various sources of contribution like opening angle of the detectors, slowing down effects within the stopper foil and deorientation effects which is especially pronounced for $\tau > 100$ ps [32].

Calculating the particle flight time using the recoil velocity and the zero distance of $43 \mu\text{m}$ results in a minimum flight time of ≈ 7 ps. Hence, we set the lower sensitivity limit of this experimental configuration at ≈ 5 ps. In the following section, the analysis procedure for the determination of the lifetimes in $^{104,106}\text{Ru}$ is explained. The analysis of the ^{104}Ru serves as consistency check of the experimental setup as well as the analysis procedure. Only the lifetime of the 3_γ^+ state was determined for the first time. All other determined lifetimes in this work confirm the literature values within the uncertainties. The spectra and fits for the data are only visualized for ^{106}Ru due to its novelty. The final lifetimes of $^{104,106}\text{Ru}$ are summarized in Table II.

A. Lifetimes in ^{104}Ru

1. Analysis of 4_γ^+ , 6_1^+ , and 3_1^- states

The observed transitions depopulating the 4_γ^+ state (609.5 and 614.2 keV), the 6_1^+ state (667.9 keV), and the 3_1^- (1612.3 keV) state, see Fig. 2, only show a shifted and no unshifted component. This indicates a lifetime too short to be measured with the properties of the experimental configuration. Therefore, an upper limit of ≈ 5 ps is set for these states i.e.,

$\tau_{4_\gamma^+} < 5\text{ps}$, $\tau_{6_1^+} < 5\text{ps}$, and $\tau_{3_1^-} < 5\text{ps}$. Although it is not an absolute result, this is an important information to account for the feeding properties of lower-lying states. The derived upper limits of less than 5 ps for the 4_γ^+ , 6_1^+ are in good agreement with previously determined lifetimes of $\tau_{4_\gamma^+} = 3.9(4)$ ps and $\tau_{6_1^+} = 1.92_{-6}^{+17}$ ps [10,24,39,40,46–48], derived as the mean of several Coulomb excitation experiments. No information about the lifetime of the 3_1^- is given in the literature.

2. Analysis of 2_γ^+ and 3_γ^+ states

The 2_γ^+ and 3_γ^+ states are only weakly populated and therefore Eq. (2) was used to obtain the lifetimes. For the lifetimes of the 2_γ^+ state, the $2_\gamma^+ \rightarrow 2_1^+$ (535.1 keV) and the $2_\gamma^+ \rightarrow 0_1^+$ (893.1 keV) have been used to determine the lifetime. In the forward ring an overlap between the $2_\gamma^+ \rightarrow 2_1^+$ (535.1 keV) and $4_1^+ \rightarrow 2_1^+$ (530.5 keV) transition is observed and the analysis using the $2_\gamma^+ \rightarrow 2_1^+$ transition was only performed for the backward ring. For the 3_γ^+ state only the $3_\gamma^+ \rightarrow 2_1^+$ transition (884.4 keV) was observed and used to obtain the lifetime. The weighted mean of the results leads to the lifetimes of $\tau_{2_\gamma^+} = 8.9(18)$ ps and $\tau_{3_\gamma^+} = 7.3(23)$ ps. To investigate possible feeding contributions for the 3_γ^+ state from higher-lying unobserved states (e.g., 5_γ^+ state as a feeder of the 3_γ^+ state) and other unobserved, unknown feeding γ rays, the simulation has been expanded to take these unobserved feeders into account. By considering the observation limit ($\approx 0.2\%$) and the observed intensities of the decay transitions of the 3_γ^+ states (see Table I), a maximum of unobserved feeding contributions is 30%. A feeding lifetime of 100 ps is assumed, which is sufficiently long to be considered as a pure long-lived feeding [15,34] with the result of $\tau_{3_\gamma^+} = 2.8(12)$ ps. The lower limit derived from the maximum feeding approach is used as the lower limit of the final lifetime. The final result is $\tau_{3_\gamma^+} = 7.3_{-57}^{+23}$ ps, where no lifetime information is available in the literature. The lifetime of the 2_γ^+ with $\tau_{2_\gamma^+} = 8.9(18)$ ps is in agreement with the mean lifetime measured by

TABLE II. Lifetimes of $^{104,106}\text{Ru}$ measured in the experiment using the Bateman equation (BE), the DDCM method, the Simulations (SIM) using Eq. (2) together with the adopted values. The literature values from Refs. [49,50] are summarized in the last column.

		Lifetime [ps]								
		Backward ring			Forward ring					
State	Decay transition [keV] [24,25]	BE	DDCM	SIM	BE	DDCM	SIM	Adopted	Lit.	
^{104}Ru	2_1^+	358.0(1)	79.5(86)	82.8(28)	79.1(66)	78.3(86)	82.4(28)	79.1(67)	80.2(66)	81.5(14) ^a
	4_1^+	530.5(1)	8.0(10)	9.0(8)	8.1(22)				8.4(13)	8.1(9) ^a
	6_1^+	667.9(3)							<5	1.92 ⁺¹⁷ ₋₆ ^a
	2_γ^+	535.1(1)			8.3(23)				} 8.9(18)	7.2(7) ^a
	2_γ^+	893.1(1)			9.2(24)			9.3(24)		
	3_γ^+	884.1(1)			9.3(50)			7.0(20)	7.3 ⁺²³ ₋₅₇	
	4_γ^+	609.5(1)							<5	3.9(4) ^a
3_1^-	1612.4(1)							<5		
^{106}Ru	2_1^+	270.1(1)	267(29)	261(12)	273(25)	282(30)	283(12)	279(26)	274(23)	264(4) ^b 375(101) ^c
	4_1^+	444.6(2)	14.6(29)	12.5(13)	13.3(15)	14.7(27)	12.4(12)	13.6(13)	13.5(15)	< 20 ^b
	6_1^+	581.1(2)			10.0 ⁺²⁵ ₋₅₅				10.0 ⁺²⁵ ₋₅₅	—
	2_γ^+	792.3(1)			13.9 ⁺⁵² ₋₄₈				13.9 ⁺⁵² ₋₄₈	10.8(43) ^b
	3_γ^+	821.5(1)			17.3 ⁺⁵² ₋₉₉				17.3 ⁺⁵² ₋₉₉	< 38 ^b
	0_2^+	720.5(1)							<5	< 8.7 ^b
	2_3^+	1122.2(1)							<5	< 19 ^b

^aFrom Refs. [10,24,39,40,46–48].

^bFrom Ref. [49].

^cFrom Ref. [50].

different Coulomb excitation experiments with a mean value of $\tau_{2_1^+} = 7.2(7)$ ps [10,24,39,40,46–48].

3. Analysis of 4_1^+ and 2_1^+ states

After the determination of the lifetime of higher-lying states, this information can be used to obtain the lifetimes of the two lowest states, namely the 4_1^+ and 2_1^+ states. The $4_1^+ \rightarrow 2_1^+$ transition (530.5 keV) has an overlap with the $2_1^+ \rightarrow 2_1^+$ transition (535.1 keV), hence, only the backward angles could be used to determine the lifetime. Here, the Bateman equation, the DDCM using the program NAPATAU [43] as well as Eq. (2) were used to determine the lifetime. The weighted mean of all results was used to adopt as lifetime and results in $\tau_{4_1^+} = 8.4(13)$ ps. The result is in good agreement with the adopted value of $\tau_{4_1^+} = 8.1(9)$ ps, given in the literature [24]. The $2_1^+ \rightarrow 0_1^+$ (358.0 keV) transition in combination with the Bateman equations, DDCM, and Eq. (2) were used to determine the lifetime of the 2_1^+ state. The final lifetime of $\tau_{2_1^+} = 80.2(66)$ ps agrees within its uncertainties to the adopted literature value of 81.5(14) ps [10,24,39,40,46–48].

B. Lifetimes in ^{106}Ru

1. Analysis of 2_3^+ and 0_2^+ states

The observed decay branches of the $2_3^+ \rightarrow 2_1^+$ state (1122.2 keV) and $0_2^+ \rightarrow 2_1^+$ state (720.5 keV) only show a shifted component, suggesting a lifetime too short to be measured

with the experimental configuration. Just as for some states in ^{104}Ru , an upper limit of 5 ps can be determined, representing the level of sensitivity in this case. No lifetime information for these two states are given in the literature.

2. Analysis of 2_γ^+ , 3_γ^+ , and 6_1^+ states

The 2_γ^+ , 3_γ^+ , and 6_1^+ states have a low population and hence Eq. (2) has been employed to obtain the lifetimes. The fits to the data are shown in Figs. 4(a) and 4(b). The resulting lifetimes are $\tau_{6_1^+} = 10.0(25)$ ps and $\tau_{3_\gamma^+} = 17.3(52)$ ps assuming no feeding. However, to investigate possible feeding contributions from unobserved higher-lying states (e.g., 8_1^+ state as a feeder of the 6_1^+ state) and other unobserved feeding γ rays, the simulation has been expanded to take these feeders into account. By considering the observation limit ($\approx 2\%$) and the observed intensities of the decay transitions of the 6_1^+ and 3_γ^+ states (see Table I), maximal contribution of unobserved feeding are in the order of 15% and 20%, respectively. Assuming a feeding lifetime of 100 ps which is sufficiently long to be considered as a pure long-lived feeding [15,34] the resulting lifetimes amount to $\tau_{6_1^+} = 6.6(21)$ ps and $\tau_{3_\gamma^+} = 11.3(39)$ ps. The lower limit of the simulation is used as the lower limit of the lifetime and the final results are $\tau_{6_1^+} = 10.0⁺²⁵₋₅₅$ ps and $\tau_{3_\gamma^+} = 17.3⁺⁵²₋₉₉$ ps. The results of the simulation with and without feeding are shown in Figs. 4(c) and 4(d). The determined value for the 3_γ^+ state is consistent with the upper limit of $\tau_{3_\gamma^+} < 38$ ps given in Ref. [49].

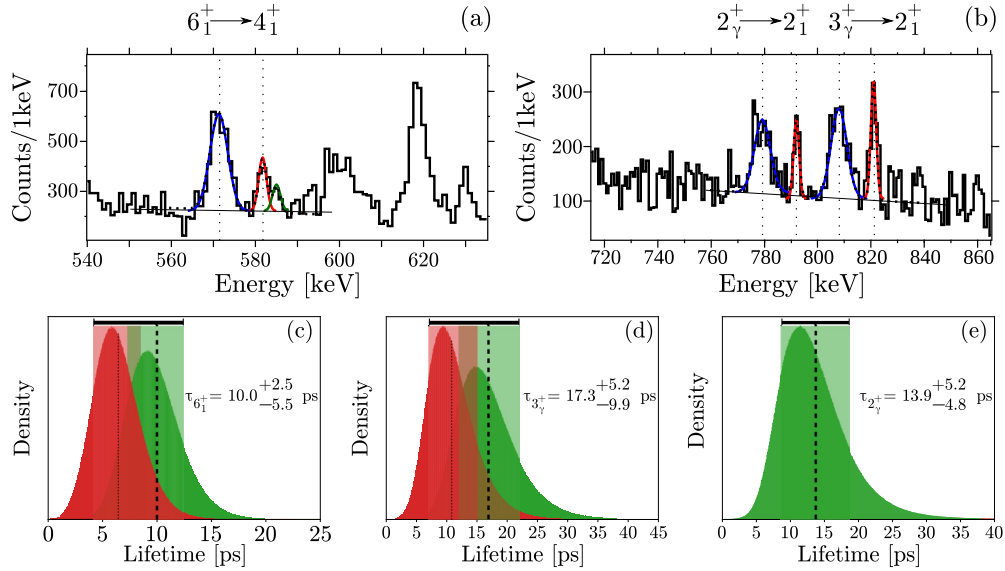


FIG. 4. (a), (b) Particle-gated γ -ray spectrum detected by the backward detectors of the $6_1^+ \rightarrow 4_1^+$ (581.1 keV), $2_\gamma^+ \rightarrow 0_1^+$ (792.3 keV), and $3_\gamma^+ \rightarrow 2_1^+$ (821.5 keV) decay transitions in ^{106}Ru with the corresponding shifted peaks. A peak at 585 keV has included in the fit procedure to account for its contribution [see panel (a)], marked in green. However, the origin of the γ ray is unclear. The γ -ray spectra of all distances are summed up due to low statistics and the fits of the shifted (blue) and unshifted (red) peaks are shown. (c)–(e) The result of the Monte Carlo simulation using Eq. (2), where no feeding is assumed (green) and the case where feeding is taken into account (red). Also the final lifetimes with the error bars are shown. See text in Sec. III B 2 for more details.

For the 2_γ^+ state only the feeding of the 3_γ^+ state has been considered which results in a final lifetime of $\tau_{2_\gamma^+} = 13.9_{-4.8}^{+5.2}$ ps. The simulation for the 2_γ^+ state with its error bar is shown in Fig. 4(e). The final result is in agreement with a previous measurement with a result of $\tau_{2_\gamma^+} = 10.8(43)$ ps [49]. The determined lifetimes and literature values are summarized in Table II.

3. Analysis of 4_1^+ and 2_1^+ states

As the lifetimes of the higher-lying states have been determined, they can be used to obtain the lifetimes of the 4_1^+ and 2_1^+ states. The evolution of the shifted and unshifted components for these states is shown in Fig. 5 for four selected distances (53, 143, 843, and 2843 μm) for the backward detectors. The solution of the Bateman equations and the DDCM using the program NAPATAU [43] are shown in the lower part of Fig. 5. For the 4_1^+ state the 444.6 keV transition ($4_1^+ \rightarrow 2_1^+$) has been used to determine the lifetime. The feeding contribution of the 6_1^+ and 3_γ^+ states have been taken into account. The final lifetime is calculated using the weighted average of the six measurements [backward and forward each Bateman equations, DDCM and simulations using Eq. (2)]. The final result for the lifetime of the 4_1^+ state is $\tau_{4_1^+} = 13.5(15)$ ps and in agreement with the upper limit of $\tau_{4_1^+} < 20$ ps given in Ref. [49].

The decay transition of the 2_1^+ state (270.1 keV) has been used to determine the lifetime. Here, the contributions of the 4_1^+ , 3_γ^+ , and 2_γ^+ states were considered. The intensity of the contribution of the $2_\gamma^+ \rightarrow 2_1^+$ (522.2 keV) transition has been calculated using the intensities given in Ref. [25]. The intensity of the 522.2 keV transition could not be determined

due to a overlap of the shifted components of the 530.5 keV ($4_1^+ \rightarrow 2_1^+$) and 535.1 keV ($2_2^+ \rightarrow 2_1^+$) transitions which are populated in the inelastic-scattering reaction of ^{104}Ru . The final lifetime is calculated the same way as discussed before and the adopted value is $\tau_{2_1^+} = 274(23)$ ps. This result is in agreement with the results of two previous lifetimes measurements, resulting in lifetimes of 264(4) ps [49] and 375(101) ps [50].

IV. CALCULATIONS

To describe the nuclei of interest calculations using the proton-neutron interacting boson model (IBM-2) [51] were performed, which are based on the microscopic energy density functional (EDF) [52–54]. The parameters of the mapped-IBM-2 Hamiltonian are determined by mapping the deformation-energy surface, which is provided by the constrained Gogny-D1M SCMF calculations [55], onto the expectation value of the mapped-IBM Hamiltonian computed with the boson condensate intrinsic wave function [56–59]. With the resulting mapped-IBM Hamiltonian energy levels and transition probabilities can be determined. In the left part of Fig. 6 the potential-energy surface (PES) of the mean-field Gogny-D1M energy density functional exhibits only a single minimum. Therefore, the single configuration of the Hamiltonian described in Ref. [56] is used. In this section, only a short description of the calculations is given. A more detailed description of the calculations is given in Ref. [56]. The Hamiltonian \hat{H}_B is defined as

$$\hat{H}_B = \epsilon \hat{n}_d + \kappa \hat{Q}_\pi \cdot \hat{Q}_\nu + \kappa' \sum_{\rho' \neq \rho} \hat{T}_{\rho\rho\rho'}, \quad (3)$$

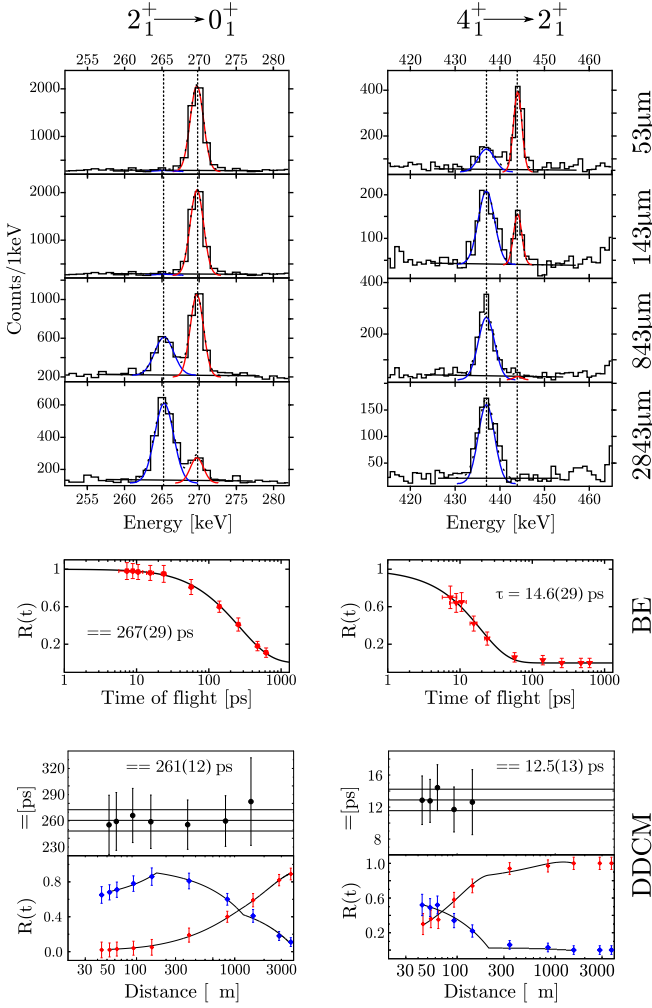


FIG. 5. The evolution of the shifted (blue) and unshifted (red) components in the backward ring for the $2_1^+ \rightarrow 0_1^+$ (left panel) and $4_1^+ \rightarrow 2_1^+$ (right panel) transitions for four selected distances, namely 53, 143, 843, and 2843 μm . Furthermore, the decay curves for the lifetimes of the 2_1^+ and 4_1^+ states using the Bateman equations to fit the data are shown. The DDC method for the 2_1^+ and 4_1^+ states using the program NAPATAU [43] for the backward angle. The individual obtained lifetimes are shown in the upper panel, and the lower panel shows the evolution of the shifted (red) and unshifted (blue) component. In addition the fit of the data is shown, which is used to obtain the derivative $\frac{d}{dx}R_i(x)$. Note that the x scale is logarithmic for the decay curves.

where $\hat{n}_d = \hat{n}_{d\nu} + \hat{n}_{d\pi}$ and $\hat{n}_{d\rho} = d_\rho^\dagger \cdot \tilde{d}_\rho$ ($\rho = \nu, \pi$) describes the d -boson number operator. The quadrupole operator is defined as $\hat{Q}_\rho = s_\rho^\dagger \tilde{d}_\rho + d_\rho^\dagger \tilde{s}_\rho + \chi_\rho [d_\rho^\dagger \times \tilde{d}_\rho]^{(2)}$ ($\rho = \nu, \pi$) and the third term is a specific three-boson interaction term with $\hat{T}_{\rho\rho\rho'} = \sum_L [d_\rho^\dagger \times d_\rho^\dagger \times d_{\rho'}^\dagger]^{(L)} \cdot [\tilde{d}_\rho \times \tilde{d}_\rho \times \tilde{d}_{\rho'}]^{(L)}$ with L being the total angular momentum in the boson system [60–62]. To calculate the electromagnetic $E2$ transition rates the following relation is used:

$$\hat{T}^{(E2)} = e_{B,\pi} \hat{Q}_\pi + e_{B,\nu} \hat{Q}_\nu, \quad (4)$$

with $e_{B,\pi}$ and $e_{B,\nu}$ being the effective charges and \hat{Q}_π and \hat{Q}_ν the quadrupole operators described before. The boson

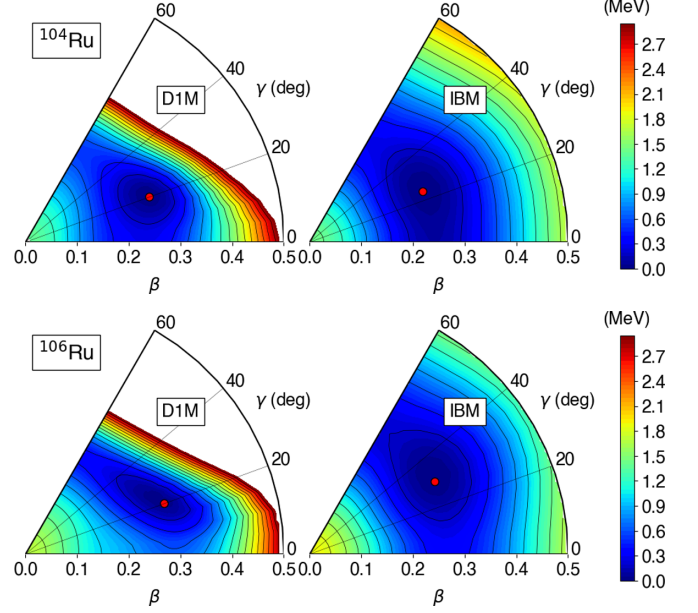


FIG. 6. Contour plot of the deformation-energy surface in the (β, γ) plane for ^{104}Ru (top) and ^{106}Ru (bottom) computed with the constrained SCMF method by using the Gogny functional D1M (left) and with the mapped IBM (right). The red dot indicates the minima of the energy surface plots and the difference between two neighboring contours is 100 keV

numbers were obtained by using the shell closures at $Z = N = 50$ and half the number of valence protons and neutrons. The $^{104,106}\text{Ru}$ nuclei have six protons and are ten (twelve) neutrons away from the closed shell. The proton boson number is $N_\pi = 3$ and the neutron boson number is $N_\nu = 5$ and $N_\nu = 6$, respectively. The minimized Hamiltonian parameters for ^{104}Ru are $\epsilon = 0.40$ MeV, $\kappa = -0.078$ MeV, $\chi_\nu = -0.10$, $\chi_\pi = -0.10$, $\kappa' = 0.25$ MeV. For ^{106}Ru the parameters $\epsilon = 0.37$ MeV, $\kappa = -0.067$ MeV, $\chi_\nu = 0.08$, $\chi_\pi = -0.05$, $\kappa' = 0.25$ MeV were used. An effective charge of $e_{B,\pi} = e_{B,\nu} = 0.108 e b$ (^{104}Ru) and $e_{B,\pi} = e_{B,\nu} = 0.104 e b$ (^{106}Ru) has been used. The effective g factors for both nuclei are $g_\nu = 0$ for neutrons and $g_\pi = 1$ for protons which are given in units of μ_N . An $E0$ operator of -0.068 fm^2 for proton and neutron bosons has been used to obtain the $\rho(E0)$ value for ^{106}Ru . In Fig. 6 the mean-field Gogny-D1M (left) and the mapped-IBM potential-energy surfaces (PESs) (right) are shown for ^{104}Ru and ^{106}Ru . For ^{104}Ru , the mean-field PES shows a distinct minimum around $\beta \approx 0.25$ and $\gamma \approx 20^\circ$ which was used to obtain the mapped-IBM parameters. The minimum in the mapped-IBM PES shows a minimum around $\beta \approx 0.25$ and $\gamma \approx 25^\circ$. In the case of ^{106}Ru , similar values are visible with a minimum around $\beta \approx 0.25$ and $\gamma \approx 20^\circ$ in the Gogny-D1M PES and $\beta \approx 0.25$ and $\gamma \approx 30^\circ$ for the mapped-IBM PES.

V. DISCUSSION

The experimental results of $^{104,106}\text{Ru}$ will be discussed and compared with the previously explained mapped-IBM calculations and to the values of the Willets-Jean γ -soft model [63] (hereafter called the γ -soft model) taken from Ref. [17]. The

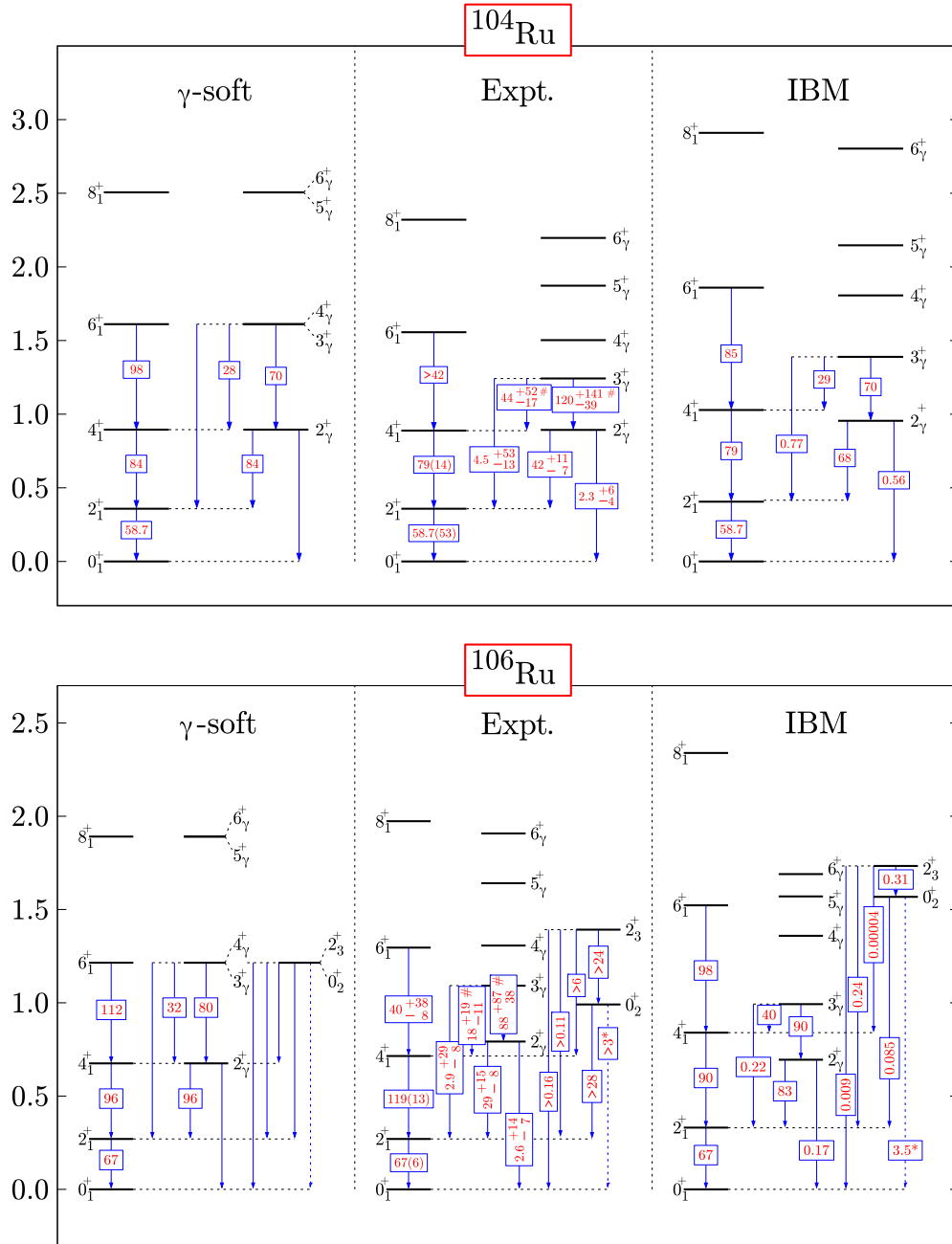


FIG. 7. The experimental (Expt.) and calculated (γ soft and mapped IBM) low energy level scheme for ^{104}Ru (top) and ^{106}Ru (bottom). The deduced $B(E2)$ transition probabilities values are placed on the corresponding arrow and are given in Weisskopf units. Due to a lack of multipole mixing ratios, some $B(E2)$ values are calculated in the limits of a pure $E2$ transitions, which are marked with #. The transition probability of the $0_2^+ \rightarrow 0_1^+$ is given in $10^3 \times \rho(E0)$.

Wilets-Jean model is similar to the $O(6)$ limit for $N \rightarrow \infty$ in the IBM [64]. The results from the calculations as well as the experimental $B(E2)$ values are visualized in Fig. 7. Additionally, all transition strengths and ratios including energies as well as transitions strength are summarized in Tables III and IV, which will be discussed in the context of triaxiality. The ratios that have been calculated are defined as follows:

$$R_{4/2} = E_{4_1^+}/E_{2_1^+}, \quad (5)$$

$$R_{6/2} = E_{6_1^+}/E_{2_1^+}, \quad (6)$$

$$R_{8/2} = E_{8_1^+}/E_{2_1^+}, \quad (7)$$

$$R_{2_{\gamma/2}} = E_{2_{\gamma}^+}/E_{2_1^+}, \quad (8)$$

$$B_{4/2} = \frac{B(E2; 4_1^+ \rightarrow 2_1^+)}{B(E2; 2_1^+ \rightarrow 0_1^+)}, \quad (9)$$

$$B_{2_\gamma/2} = \frac{B(E2; 2_\gamma^+ \rightarrow 2_1^+)}{B(E2; 2_1^+ \rightarrow 0_1^+)}, \quad (10)$$

$$B'_{2_\gamma/2} = \frac{B(E2; 2_\gamma^+ \rightarrow 2_1^+)}{B(E2; 2_\gamma^+ \rightarrow 0_1^+)}. \quad (11)$$

Due to asymmetric uncertainties, the lower and upper limits of the last two ratios ($B_{2_\gamma/2}$ and $B'_{2_\gamma/2}$) were calculated using

TABLE III. The experimental, the mapped-IBM calculated and γ -soft model (taken from Ref. [17]) reduced transition probabilities of ^{104}Ru . The branching ratios are taken from the Nuclear Data Sheets [24]. For transitions with unknown multipole mixing ratios, the corresponding transition strength are calculated in the limit of pure $E2$ and $M1$ transitions and are marked with an asterisk. The $B(E2)$, $B(E1)$, and $B(M2)$ values are given in W.u. and the $B(M1)$ values are given in $10^{-4}\mu_N^2$. Furthermore, the ratios defined in Eqs. (5)–(11), were calculated for a comparison with the mapped-IBM and the γ -soft limit to discuss triaxiality.

Reduced transition strength	Experiment	IBM	γ soft [17]
$B(E2; 2_1^+ \rightarrow 0_1^+)$	58.7(53)	58.7	58.7
$B(E2; 4_1^+ \rightarrow 2_1^+)$	79(14)	79	84
$B(E2; 6_1^+ \rightarrow 4_1^+)$	>42	85	98
$B(E2; 2_\gamma^+ \rightarrow 0_1^+)$	2.3^{+6}_{-4}	0.56	
$B(E2; 2_\gamma^+ \rightarrow 2_1^+)^a$	42^{+11}_{-7}	68	84
$B(M1; 2_\gamma^+ \rightarrow 2_1^+)^a$	1.9^{+34}_{-10}	0.66	
$B(E2; 3_\gamma^+ \rightarrow 2_1^+)^b$	4.5^{+53}_{-13}	0.77	
$B(M1; 3_\gamma^+ \rightarrow 2_1^+)^b$	7.3^{+88}_{-29}	9.7	
$B(E2; 3_\gamma^+ \rightarrow 4_1^+)^*$	44^{+52}_{-17}	29	28
$B(M1; 3_\gamma^+ \rightarrow 4_1^+)^*$	110^{+130}_{-40}	4.4	
$B(E2; 3_\gamma^+ \rightarrow 2_\gamma^+)^*$	120^{+141}_{-39}	70	70
$B(M1; 3_\gamma^+ \rightarrow 2_\gamma^+)^*$	300^{+350}_{-100}	1.7	
$B(E2; 4_\gamma^+ \rightarrow 2_1^+)$	>0.3	0.068	
$B(E2; 4_\gamma^+ \rightarrow 4_1^+)^*$	>21	27	46
$B(M1; 4_\gamma^+ \rightarrow 4_1^+)^*$	>160	30	
$B(E2; 4_\gamma^+ \rightarrow 2_\gamma^+)$	>37	34	51
$B(E1; 3_1^- \rightarrow 2_1^+)^c$	$>2 \times 10^{-5} / >8 \cdot 10^{-7}$		
$B(M2; 3_1^- \rightarrow 2_1^+)^c$	$>4 \times 10^{-2} / >36$		
$R_{4/2} = E_{4_1^+}/E_{2_1^+}$	2.48(1)	2.53	2.5
$R_{6/2} = E_{6_1^+}/E_{2_1^+}$	4.35(1)	4.58	4.5
$R_{8/2} = E_{8_1^+}/E_{2_1^+}$	6.48(1)	7.17	7
$R_{2_\gamma/2} = E_{2_\gamma^+}/E_{2_1^+}$	2.49(1)	2.35	2.5
$B_{4/2} = \frac{B(E2; 4_1^+ \rightarrow 2_1^+)}{B(E2; 2_1^+ \rightarrow 0_1^+)}$	1.35(27)	1.35	1.43
$B_{2_\gamma/2} = \frac{B(E2; 2_\gamma^+ \rightarrow 2_1^+)}{B(E2; 2_1^+ \rightarrow 0_1^+)}$	0.73^{+7}_{-20} ^d	1.18	1.43
$B'_{2_\gamma/2} = \frac{B(E2; 2_\gamma^+ \rightarrow 2_1^+)}{B(E2; 2_\gamma^+ \rightarrow 0_1^+)}$	22^{+22d}_{-21}	121	∞

^aA $M1/E2$ mixing ratio of $\delta = -36^{+14}_{-54}$ was used [65].

^bA $M1/E2$ mixing ratio of $\delta = -3.2(4)$ was used [65].

^cA $E1/M2$ mixing ratio of $\delta = 0.01$ or 5.2^{+18}_{-11} was used [65]. However, the results with the large mixing ratio of $\delta = 5.2^{+18}_{-11}$ seem unreasonable.

^dDue to asymmetric uncertainties, the error is calculated using a maximum value estimation. See text for more details.

the maximum value of the numerator and the minimum of the denominator as the upper limit and vice versa for the lower limit. Note that this does not result in an 1σ error.

A. ^{104}Ru

1. Energy levels

Level energies and $B(E2)$ transition probabilities derived for the experiment and from the calculations of the mapped-IBM and γ -soft model for ^{104}Ru are shown in Fig. 7. The level energies of the 2_1^+ and 4_1^+ are well described by both calculations. The energy levels of the 6_1^+ and 8_1^+ state are overestimated by both calculations, where the γ -soft calculations has a smaller deviation. The energy levels of the γ band are slightly overestimated by the γ -soft calculations. However, the clustering of the $(3_\gamma^+, 4_\gamma^+)$ and $(5_\gamma^+, 6_\gamma^+)$ states

TABLE IV. Same as Table III but for ^{106}Ru . The branching ratios are taken from the Nuclear Data Sheets [25].

Transition strength	Experiment	IBM	γ soft [17]
$B(E2; 2_1^+ \rightarrow 0_1^+)$	67(6)	67	67
$B(E2; 4_1^+ \rightarrow 2_1^+)$	116(14)	90	96
$B(E2; 6_1^+ \rightarrow 4_1^+)$	40^{+38}_{-8}	98	112
$B(E2; 2_\gamma^+ \rightarrow 0_1^+)$	2.6^{+14}_{-7}	0.17	
$B(E2; 2_\gamma^+ \rightarrow 2_1^+)^a$	29^{+15}_{-8}	83	96
$B(M1; 2_\gamma^+ \rightarrow 2_1^+)^a$	3.5^{+36}_{-15}	12	
$B(E2; 3_\gamma^+ \rightarrow 2_1^+)^b$	2.9^{+29}_{-8}	0.22	
$B(M1; 3_\gamma^+ \rightarrow 2_1^+)^b$	3.3^{+61}_{-18}	7.5	
$B(E2; 3_\gamma^+ \rightarrow 4_1^+)^*$	18^{+19}_{-11}	40	32
$B(M1; 3_\gamma^+ \rightarrow 4_1^+)^*$	5.3^{+57}_{-33}	2.1	
$B(E2; 3_\gamma^+ \rightarrow 2_\gamma^+)^*$	88^{+87}_{-38}	90	80
$B(M1; 3_\gamma^+ \rightarrow 2_\gamma^+)^*$	160^{+160}_{-70}	26	
$B(E2; 2_3^+ \rightarrow 0_1^+)$	>0.16	0.009	
$B(E2; 2_3^+ \rightarrow 2_1^+)^c$	>0.11	0.24	
$B(M1; 2_3^+ \rightarrow 2_1^+)^c$	>49	2.6	
$B(E2; 2_3^+ \rightarrow 4_1^+)$	>6	0.000039	0
$B(E2; 2_3^+ \rightarrow 0_2^+)$	>24	0.31	45
$\rho(E0; 0_2^+ \rightarrow 0_1^+)^d$	>3	3.5	
$B(E2; 0_2^+ \rightarrow 2_1^+)$	>28	0.085	
$R_{4/2} = E_{4_1^+}/E_{2_1^+}$	2.65(1)	2.54	2.5
$R_{6/2} = E_{6_1^+}/E_{2_1^+}$	4.80(1)	4.60	4.5
$R_{8/2} = E_{8_1^+}/E_{2_1^+}$	7.31(1)	7.07	7
$R_{2_\gamma/2} = E_{2_\gamma^+}/E_{2_1^+}$	2.93(1)	2.10	2.5
$B_{4/2} = \frac{B(E2; 4_1^+ \rightarrow 2_1^+)}{B(E2; 2_1^+ \rightarrow 0_1^+)}$	1.82(29)	1.33	1.43
$B_{2_\gamma/2} = \frac{B(E2; 2_\gamma^+ \rightarrow 2_1^+)}{B(E2; 2_1^+ \rightarrow 0_1^+)}$	0.45^{+24e}_{-13}	1.24	1.43
$B'_{2_\gamma/2} = \frac{B(E2; 2_\gamma^+ \rightarrow 2_1^+)}{B(E2; 2_\gamma^+ \rightarrow 0_1^+)}$	11.5^{+127e}_{-60}	512.5	∞

^aA $M1/E2$ mixing ratio of $\delta = 7.1^{+16}_{-11}$ was used [41].

^bA $M1/E2$ mixing ratio of $\delta = -3.8^{+9}_{-16}$ was used [41].

^cA $M1/E2$ mixing ratio of $\delta = -0.24^{+13}_{-12}$ was used [41].

^dThe electric monopole transition strength between 0^+ states is given in $10^3 \times \rho^2(E0)$ and were calculated using the method explained in Refs. [66,67].

^eDue to asymmetric uncertainties, the error is calculated using a maximum value estimation. See text for more details.

resembles the expectations from the γ -soft model. Although the mapped-IBM predicts the states of the γ band higher than the experimental observations, it gives a reasonable description of these states and breaks down starting with 6_γ^+ state.

The experimental ratios of the ground-state band (see Table III), namely, the $R_{4/2} = 2.48(1)$, $R_{6/2} = 4.35(1)$, and $R_{8/2} = 6.48(1)$ are overestimated by the mapped-IBM by a small margin and lie closer to the ratios of the γ -soft rotational limits which are 2.5, 4.5, and 7.

The experimental $R_{2_\gamma/2} = E_{2_\gamma^+}/E_{2_1^+}$ ratio cannot be reproduced by the mapped-IBM but is in good agreement with the γ -soft limit which has a value of 2.5. The experimentally observed spacing in the sequence 2_γ^+ , 3_γ^+ , 4_γ^+ , 5_γ^+ , and 6_γ^+ states of the γ band is rather constant. This is supported by the staggering parameters $S(4) = -0.25(1)$, $S(5) = 0.31(1)$, and $S(6) = -0.13(1)$ that lie around zero (see Fig. 1), which translates to a constant spacing between the states. However, these values show weak signs of a γ -soft type of nucleus where the staggering parameter is negative for even spins and positive for odd spins [21]. Although the mapped-IBM calculations overestimate all of the level energies, the spacing in the γ band is also constant with the exception of the 6_γ^+ state. From an energy-level point of view, the ^{104}Ru nucleus show signs of γ softness which is supported by the prediction of the γ -soft model and indicated by the mapped-IBM calculations.

2. Reduced transition probabilities

To further discuss γ softness in this nucleus, a closer look to the reduced transition rates is necessary. The mapped-IBM and γ -soft calculations are adjusted to the experimental $B(E2; 2_1^+ \rightarrow 0_1^+)$ value. The $B(E2; 4_1^+ \rightarrow 2_1^+)$ value is in good agreement with both calculations within the given uncertainties. The mapped-IBM $B(E2; 6_1^+ \rightarrow 4_1^+)$ value of 85 W.u. is able to describe the experimental lower limit of 42 W.u. of this work. In comparison, the adopted literature value of the $B(E2; 6_1^+ \rightarrow 4_1^+) = 110_{-9}^{+4}$ W.u. [10] is lower than the prediction by the IBM. However, the literature value has a very good agreement with the expected at the γ -soft limit. The $B(E2; 2_\gamma^+ \rightarrow 0_1^+)$ value is underestimated and the $B(E2; 2_\gamma^+ \rightarrow 2_1^+)$ value is overestimated by both theoretical approaches. For the $E2$ transitions decaying from the 3_γ^+ state, all the values are predict to low by both calculations. Note that the $B(E2; 3_\gamma^+ \rightarrow 4_1^+)$ strength and $B(E2; 3_\gamma^+ \rightarrow 2_\gamma^+)$ strength are calculated assuming a pure $E2$ transition due to a lack of information of multipole mixing ratios. Hence, these experimental values might be significantly lower depending on the mixing ratio. The γ -soft model as well as the mapped-IBM are capable to describe the $B_{4/2}$ ratio within the uncertainties in contrast to the overestimation of the $B_{2_\gamma/2}$ and $B'_{2_\gamma/2}$ ratios.

B. ^{106}Ru

1. Energy levels

Level energies and $B(E2)$ transition probabilities derived for the experiment and from the calculations of the mapped-IBM and γ -soft model for ^{106}Ru are shown in Fig. 7. The level energies of the 2_1^+ and 4_1^+ are well described by both calculations. But for both calculations, the energy levels of

the 6_1^+ and 8_1^+ state are overestimated, where the γ -soft calculations have a smaller deviation. The γ -soft model is able to predict a reasonable energy level for the 2_γ^+ state and 4_γ^+ state. Note that the mapped-IBM calculations predict the 2_γ^+ state below the 4_1^+ state. This is an indicator that can be found in a rigid triaxial deformation. The 3_γ^+ , 5_γ^+ , and 6_γ^+ states in the γ -soft calculations are overestimated while the mapped-IBM calculation underestimates the experimental energy levels of these states. The $R_{4/2}$, $R_{6/2}$, $R_{8/2}$, and $R_{2_\gamma/2}$ ratios for the experiment, for the mapped-IBM calculations and for a γ -soft nucleus, according to the Ref. [17], are summarized in Table IV. The experimental ratios for the yrast band are predicted with reasonable accuracy by both approaches. The $R_{2_\gamma/2}$ ratios including the 2_γ^+ of the γ band cannot be predicted by either calculation.

2. Reduced transition probabilities

In Table IV the experimental $B(E2)$ and $B(M1)$ values are summarized and compared with the results from the mapped-IBM calculations and the γ -soft calculations. In Fig. 7 the $B(E2)$ strengths given in Weisskopf units are shown for the experiment, the mapped-IBM calculations, and the γ -soft calculations. The calculations have been adjusted to reproduce the $B(E2; 2_1^+ \rightarrow 0_1^+)$ transition strength. The mapped-IBM and γ -soft value for the $B(E2; 4_1^+ \rightarrow 2_1^+)$ strength lies within the 3σ range of the experimental observation. The $B(E2; 6_1^+ \rightarrow 4_1^+)$ on the other hand is overestimated by both calculations, where one has to note the large uncertainties of the experimental transitions strength. The $M1/E2$ mixed $2_\gamma^+ \rightarrow 2_1^+$ transition has been calculated using a multipole mixing ratio of $\delta = 7.1_{-1.1}^{+1.5}$ [41] and suggests a strong $E2$ component. Both calculations overestimate the $B(E2)$ value and the mapped-IBM calculation underestimates the corresponding $B(M1)$ value. The mapped-IBM $B(E2; 2_\gamma^+ \rightarrow 0_1^+)$ strength is an order of magnitude smaller than the experimental value, while the γ -soft limit predicts a vanishing transition strength. The experimental $B(E2; 3_\gamma^+ \rightarrow 4_1^+)$ and $B(E2; 3_\gamma^+ \rightarrow 2_\gamma^+)$ values are described by both theoretical approaches within the uncertainties. Note that both values were calculated assuming a pure $E2$ transition due to the lack of information about the mixing ratios. For the remaining $3_\gamma^+ \rightarrow 2_1^+$ transition, the mapped-IBM calculations is not capable of describing the value while the γ -soft approach is not capable of calculating a value. The $B_{4/2}$ ratio calculated using the mapped-IBM and the γ -soft limit lies within the 2σ interval of the experimental ratio. The experimental ratio lies closer to the vibrational limit ($B_{4/2} = 2$), whereas the calculated ratios suggest a more rotational or γ -soft behavior with both limits being $B_{4/2} = 1.43$. The calculated $B_{2_\gamma/2}$ value slightly overestimate the experimental ratio. The experimental $B'_{2_\gamma/2}$ value is order(s) of magnitudes smaller than the calculated values.

C. γ softness in $^{104,106}\text{Ru}$

Both nuclei are located in a region where triaxiality and γ softness have been suggested by different works [11–16,20,30,68,69]. First, the $R_{4/2}$ ratio for this two nuclei in

particular are around the typical γ -soft ratio of ≈ 2.5 [70]. The corresponding molybdenum and palladium isotones of ^{104}Ru , i.e., ^{102}Mo and ^{106}Pd , have similar ratios. The higher Z isotone of ^{106}Ru , namely, ^{108}Pd shows a similar ratio, whereas ^{104}Mo is closer to a ratio of $R_{4/2} \approx 3$ [24]. Furthermore, the energy levels of the 4_1^+ and 2_γ^+ states in $^{104,106}\text{Ru}$ are almost equal, which is a hint for triaxiality. Note that the mapped-IBM calculations predict the 2_γ^+ state below the 4_1^+ state for both nuclei, which can be found in a rigid triaxial deformation. Although the even-odd staggering is not well pronounced, it reveals signs of γ softness (see Fig. 1). This is also supported by the neighboring ^{102}Ru and ^{108}Ru isotopes which have similar staggering parameter $S(4) \approx -0.3$, $S(5) \approx 0.35$, $S(6) \approx -0.15$, and $S(7) \approx 0.3$ values. The same holds for the corresponding isotones $^{106,108}\text{Pd}$ and ^{102}Mo , but not for ^{104}Mo .

The mapped-IBM calculation delivers a capable description of the low-spin 2_γ^+ , 3_γ^+ , and 4_γ^+ states of the γ band in $^{104,106}\text{Ru}$. As shown in Fig. 6, the corresponding potential-energy surfaces show pronounced γ -soft and triaxial minima for both nuclei. The lifetimes of the 2_γ^+ state in both nuclei revealed a more collective $B(E2; 2_\gamma^+ \rightarrow 2_1^+)$ strength as well as an almost noncollective $B(E2; 2_\gamma^+ \rightarrow 0_1^+)$ transition probability. Both transition probabilities are comparable to the mapped-IBM calculation and the γ -soft calculations. The experimental transition rates of the 3_γ^+ state are in agreement with both calculations showing a large $B(E2; 3_\gamma^+ \rightarrow 2_\gamma^+)$ and a small $B(E2; 3_\gamma^+ \rightarrow 2_1^+)$ value.

For the investigation of γ softness, the inclusion of quadrupole moments can be insightful [71]. Therefore, the quadrupole moments up to the sixth order of the mapped-IBM approach have been calculated. They are defined as a relative dimensionless shape invariant parameter according to the following relation [71]:

$$K_n = \frac{q_n}{q_2^{n/2}} \text{ for } n \in \{3, 4, 5, 6\}, \quad (12)$$

where q_n are the quadrupole moment of the n th order. The shape invariant K_n can be used to determine the fluctuation of the effective deformation and are defined as [71]

$$\sigma_\beta = K_4 - 1, \quad (13)$$

$$\sigma_\gamma = K_6 - K_3^2. \quad (14)$$

A more detailed description of the calculation of these values is given in Ref. [71]. The resulting shape invariant of the mapped-IBM calculations are summarized in Table V and compared with the dynamical symmetry limits of the mapped IBM, namely, the U(5) (spherical vibrator) and γ -soft limit. The K_3 shape invariant is rather small for both nuclei. K_4 is an important invariant to distinguish between the U(5) and γ -soft symmetry, where the mapped-IBM calculations lie close to the γ -soft value for both nuclei. The same holds for the K_6 invariant which is significantly closer to the γ -soft limit compared with the U(5) limit. For both fluctuations of the effective deformation (σ_β and σ_γ) the values are better described by the γ -soft limit as well. The calculated effective β_{eff} and γ_{eff} given in Table V are consistent with the global

TABLE V. The quadrupole shape invariant K_n generated from the IBM calculations for $^{104,106}\text{Ru}$. For comparison the U(5) symmetry as well as the γ -soft limit is shown.

	$^{104}\text{Ru}_{\text{IBM}}$	$^{106}\text{Ru}_{\text{IBM}}$	γ soft	U(5)
q_2 [$e^2 \text{b}^2$]	0.814	1.011		
K_3	0.157	0.074	0	0
K_4	1.009	1.010	1	1.4
K_5	0.192	0.068	0	0
K_6	0.278	0.264	$\frac{1}{3}$	0.84
β_{eff}	0.269	0.297		
γ_{eff}	27.0°	31.6°	30.0°	30.0°
σ_β	0.009	0.009	0	0.4
σ_γ	0.253	0.257	$\frac{1}{3}$	0.84

minima of the potential-energy surfaces. In general, most of the γ -soft invariant are capable of describing the properties of $^{104,106}\text{Ru}$. This fact in addition with the staggering parameter and the reduced transition strength that are well described by the γ -soft limit, suggest that both nuclei show signatures of softness in the γ degree of freedom.

VI. CONCLUSIONS

The lifetimes of the 2_1^+ , 4_1^+ , 2_γ^+ , 3_γ^+ states and upper limits for the lifetimes of the 6_1^+ , 4_γ^+ , and 3_1^- states in ^{104}Ru were measured using the RDDS technique. Furthermore, the lifetimes of the 2_1^+ , 4_1^+ , 6_1^+ , 2_γ^+ , 3_γ^+ states and upper limits for the lifetimes of the 0_2^+ and 2_3^+ states were determined in ^{106}Ru . The results were compared with previous measurements and to a mapped-IBM calculation which is based on a microscopic energy density functional and to the γ -soft limit. The mapped IBM describes the energy levels and transition strength of the ground-state band and the low-spin states of the γ band for both nuclei with reasonable accuracy. The deduced transition strength of the γ band in combination with the energy level and the energy spacing within the γ band reveal signatures of γ -soft behavior in $^{104,106}\text{Ru}$. This is supported by the mapped-IBM calculations which show a broad minimum at $\gamma \approx 30^\circ$ that spreads in the γ degree of freedom. The even odd staggering underlines the γ soft behavior and pointing towards slight γ softness. The transition strengths were compared with the γ -soft limit which further manifest the γ softness of these nuclei. Higher-order quadrupole moments were used to calculated shape invariants. These invariants are used as signatures of triaxiality and also indicated γ softness in $^{104,106}\text{Ru}$.

ACKNOWLEDGMENTS

We thank the operator team of the IKP FN Tandem accelerator for the professional support during the experiment. A.E., V.K., and M.B. acknowledge the support by the BMBF under Grant No. 05P15PKFNA. K.N. acknowledges the support by the Tenure Track Pilot Programme of the Croatian Science Foundation and the École Polytechnique Fédérale de Lausanne, and the Project TTP-2018-07-3554 Exotic Nuclear Structure and Dynamics, with funds of the Croatian-Swiss Research Programme.

- [1] P. Cejnar, J. Jolie, and R. F. Casten, *Rev. Mod. Phys.* **82**, 2155 (2010).
- [2] K. Heyde and J. L. Wood, *Rev. Mod. Phys.* **83**, 1467 (2011).
- [3] P. E. Garrett, M. Zielińska, and E. Clément, *Prog. Part. Nucl. Phys.* **124**, 103931 (2022).
- [4] A. Esmaylzadeh, J.-M. Régis, Y. H. Kim, U. Köster, J. Jolie, V. Karayonchev, L. Knafla, K. Nomura, L. M. Robledo, and R. Rodríguez-Guzmán, *Phys. Rev. C* **100**, 064309 (2019).
- [5] E. Clément, M. Zielińska, A. Görgen, W. Korten, S. Péru, J. Libert, H. Goutte, S. Hilaire, B. Bastin, C. Bauer, A. Blazhev, N. Bree, B. Bruyneel, P. A. Butler, J. Butterworth, P. Delahaye, A. Dijon, D. T. Doherty, A. Ekström, C. Fitzpatrick *et al.*, *Phys. Rev. Lett.* **116**, 022701 (2016).
- [6] J.-M. Régis, J. Jolie, N. Saed-Samii, N. Warr, M. Pfeiffer, A. Blanc, M. Jentschel, U. Köster, P. Mutti, T. Soldner, G. S. Simpson, F. Drouet, A. Vancraeynest, G. de France, E. Clément, O. Stezowski, C. A. Ur, W. Urban, P. H. Regan, Z. Podolyák *et al.*, *Phys. Rev. C* **95**, 054319 (2017).
- [7] P. E. Garrett, K. L. Green, and J. L. Wood, *Phys. Rev. C* **78**, 044307 (2008).
- [8] P. E. Garrett, T. R. Rodríguez, A. D. Varela, K. L. Green, J. Bangay, A. Finlay, R. A. E. Austin, G. C. Ball, D. S. Bandyopadhyay, V. Bildstein, S. Colosimo, D. S. Cross, G. A. Demand, P. Finlay, A. B. Garnsworthy, G. F. Grinyer, G. Hackman, B. Jigmeddorj, J. Jolie, W. D. Kulp *et al.*, *Phys. Rev. Lett.* **123**, 142502 (2019).
- [9] L. Svensson, C. Fahlander, L. Hasselgren, A. Bäcklin, L. Westerberg, D. Cline, T. Czosnyka, C. Wu, R. Diamond, and H. Kluge, *Nucl. Phys. A* **584**, 547 (1995).
- [10] J. Srebrny, T. Czosnyka, C. Droste, S. Rohoziński, L. Próchniak, K. Zajac, K. Pomorski, D. Cline, C. Wu, A. Bäcklin, L. Hasselgren, R. Diamond, D. Habs, H. Körner, F. Stephens, C. Baktash, and R. Kostecki, *Nucl. Phys. A* **766**, 25 (2006).
- [11] Y. Luo, S. Zhu, J. Hamilton, J. Rasmussen, A. Ramayya, C. Goodin, K. Li, J. Hwang, D. Almeded, S. Frauendorf, V. Dimitrov, J. ye Zhang, X. Che, Z. Jang, I. Stefanescu, A. Gelberg, G. Ter-Akopian, A. Daniel, M. Stoyer, R. Donangelo *et al.*, *Phys. Lett. B* **670**, 307 (2009).
- [12] D. Doherty, J. Allmond, R. Janssens, W. Korten, S. Zhu, M. Zielińska, D. Radford, A. Ayangeakaa, B. Bucher, J. Batchelder, C. Beausang, C. Campbell, M. Carpenter, D. Cline, H. Crawford, H. David, J. Delaroche, C. Dickerson, P. Fallon, A. Galindo-Uribarri *et al.*, *Phys. Lett. B* **766**, 334 (2017).
- [13] P.-A. Söderström, G. Lorusso, H. Watanabe, S. Nishimura, P. Doornenbal, G. Thiamova, F. Browne, G. Gey, H. S. Jung, T. Sumikama, J. Taprogge, Z. Vajta, J. Wu, Z. Y. Xu, H. Baba, G. Benzoni, K. Y. Chae, F. C. L. Crespi, N. Fukuda, R. Gerhäuser *et al.*, *Phys. Rev. C* **88**, 024301 (2013).
- [14] I. Stefanescu, A. Gelberg, J. Jolie, P. Van Isacker, P. von Brentano, Y. Luo, S. Zhu, J. Rasmussen, J. Hamilton, A. Ramayya, and X. Che, *Nucl. Phys. A* **789**, 125 (2007).
- [15] A. Esmaylzadeh, V. Karayonchev, G. Häfner, J. Jolie, M. Beckers, A. Blazhev, A. Dewald, C. Fransen, A. Goldkuhle, L. Knafla, and C. Müller-Gatermann, *Phys. Rev. C* **103**, 054324 (2021).
- [16] A. Esmaylzadeh, V. Karayonchev, K. Nomura, J. Jolie, M. Beckers, A. Blazhev, A. Dewald, C. Fransen, R.-B. Gerst, G. Häfner, A. Harter, L. Knafla, M. Ley, L. M. Robledo, R. Rodríguez-Guzmán, and M. Rudigier, *Phys. Rev. C* **104**, 064314 (2021).
- [17] L. Wilets and M. Jean, *Phys. Rev.* **102**, 788 (1956).
- [18] A. Davydov and G. Filippov, *Nucl. Phys.* **8**, 237 (1958).
- [19] A. Davydov and V. Rostovsky, *Nucl. Phys.* **12**, 58 (1959).
- [20] A. S. Davydov and V. S. Rostovskii, *J. Exptl. Theoret. Phys.* **36**, 1788 (1959) [*Sov. Phys. JETP* **36** (1959)].
- [21] N. Zamfir and R. Casten, *Phys. Lett. B* **260**, 265 (1991).
- [22] B. Singh and J. Chen, *Nucl. Data Sheets* **172**, 1 (2021).
- [23] D. De Frenne, *Nucl. Data Sheets* **110**, 1745 (2009).
- [24] J. Blachot, *Nucl. Data Sheets* **108**, 2035 (2007).
- [25] D. De Frenne and A. Negret, *Nucl. Data Sheets* **109**, 943 (2008).
- [26] J. Blachot, *Nucl. Data Sheets* **62**, 803 (1991).
- [27] G. Gürdal and F. Kondev, *Nucl. Data Sheets* **113**, 1315 (2012).
- [28] S. Lalkovski and F. Kondev, *Nucl. Data Sheets* **124**, 157 (2015).
- [29] D. Ralet, S. Pietri, T. Rodríguez, M. Alaqael, T. Alexander, N. Alkhomashi, F. Ameil, T. Arici, A. Ataç, R. Avigo, T. Bäck, D. Bazzacco, B. Birkenbach, P. Boutachkov, B. Bruyneel, A. M. Bruce, F. Camera, B. Cederwall, S. Ceruti, E. Clément, and M. Zielinska (for the PreSPEC and AGATA Collaborations), *Phys. Rev. C* **95**, 034320 (2017).
- [30] J. Ha, T. Sumikama, F. Browne, N. Hinohara, A. M. Bruce, S. Choi, I. Nishizuka, S. Nishimura, P. Doornenbal, G. Lorusso, P.-A. Söderström, H. Watanabe, R. Daido, Z. Patel, S. Rice, L. Sinclair, J. Wu, Z. Y. Xu, A. Yagi, H. Baba *et al.*, *Phys. Rev. C* **101**, 044311 (2020).
- [31] J. Chen and B. Singh, *Nucl. Data Sheets* **164**, 1 (2020).
- [32] A. Dewald, O. Möller, and P. Petkov, *Prog. Part. Nucl. Phys.* **67**, 786 (2012).
- [33] V. Karayonchev, J. Jolie, A. Blazhev, A. Dewald, A. Esmaylzadeh, C. Fransen, G. Häfner, L. Knafla, J. Litzinger, C. Müller-Gatermann, J.-M. Régis, K. Schomacker, A. Vogt, N. Warr, A. Leviatan, and N. Gavrielov, *Phys. Rev. C* **102**, 064314 (2020).
- [34] M. Beckers, C. Müller-Gatermann, A. Blazhev, T. Braunroth, A. Dewald, C. Fransen, A. Goldkuhle, L. Kornwebel, J. Litzinger, F. von Spee, and K.-O. Zell, *Phys. Rev. C* **102**, 014324 (2020).
- [35] A. Dewald, S. Harissopulos, and P. von Brentano, *Z. Phys. A: At. Nucl.* **334**, 163 (1989).
- [36] T. Alexander and A. Bell, *Nucl. Instrum. Methods* **81**, 22 (1970).
- [37] M. Beckers, A. Dewald, C. Fransen, L. Kornwebel, C.-D. Lakenbrink, and F. von Spee, *Nucl. Inst. Meth. Phys. Res. Sec. A* **1042**, 167416 (2022).
- [38] J. Koenig, H. Bohn, T. Faestermann, P. Kienle, H. J. Körner, W. A. Mayer, D. Pereira, K. E. Rehm, and H. J. Scheerer, *Phys. Rev. C* **24**, 2076 (1981).
- [39] S. Landsberger, R. Lecomte, P. Paradis, and S. Monaro, *Phys. Rev. C* **21**, 588 (1980).
- [40] F. McGowan, R. Robinson, P. Stelson, and W. Milner, *Nucl. Phys. A* **113**, 529 (1968).
- [41] J. Stachel, N. Kaffrell, N. Trautmann, K. Brodén, G. Skarnemark, and D. Eriksen, *Z. Phys. A: Hadrons Nuclei* **316**, 105 (1984).
- [42] H. Bateman, *Proc. Camb. Philos. Soc. Math. Phys. Sci.* **15**, 423 (1910).
- [43] B. Saha, Ph.D. thesis, Universität zu Köln, 2004, <https://kups.ub.uni-koeln.de/1246/>.
- [44] J. Litzinger, A. Blazhev, A. Dewald, F. Didierjean, G. Duchêne, C. Fransen, R. Lozeva, K. Sieja, D. Verney, G. de Angelis, D.

- Bazzacco, B. Birkenbach, S. Bottoni, A. Bracco, T. Braunroth, B. Cederwall, L. Corradi, F. C. L. Crespi, P. Désesquelles, J. Eberth *et al.*, *Phys. Rev. C* **92**, 064322 (2015).
- [45] J. Litzinger, Ph.D. thesis, Universität zu Köln, 2018, <https://kups.uni-koeln.de/8987/>.
- [46] J. Stachel, P. Hill, N. Kaffrell, H. Emling, H. Grein, E. Grosse, C. Michel, H.-J. Wollersheim, D. Schwalm, S. Brüssermann, and F. May, *Nucl. Phys. A* **419**, 589 (1984).
- [47] P. H. Stelson and F. K. McGowan, *Phys. Rev.* **110**, 489 (1958).
- [48] G. M. Temmer and N. P. Heydenburg, *Phys. Rev.* **104**, 967 (1956).
- [49] M. Sanchez-Vega, H. Mach, R. B. E. Taylor, B. Fogelberg, A. Lindroth, A. J. Aas, P. Dendooven, A. Honkanen, M. Huhta, G. Lhersonneau, M. Oinonen, J. M. Parmonen, H. Penttilä, J. Åystö, J. R. Persson, and J. Kurpeta, *Eur. Phys. J. A* **35**, 159 (2008).
- [50] S. Schoedder, G. Lhersonneau, A. Wöhr, G. Skarnemark, J. Alstad, A. Nähler, K. Eberhardt, J. Åystö, N. Trautmann, and K. L. Kratz, *Z. Phys. A: Hadrons Nucl.* **352**, 237 (1995).
- [51] F. Iachello and A. Arima, in *The Interacting Boson Model*, Cambridge Monographs on Mathematical Physics (Cambridge University Press, Cambridge, 1987).
- [52] M. Bender, P.-H. Heenen, and P.-G. Reinhard, *Rev. Mod. Phys.* **75**, 121 (2003).
- [53] T. Nikšić, D. Vretenar, and P. Ring, *Prog. Part. Nucl. Phys.* **66**, 519 (2011).
- [54] L. M. Robledo, T. R. Rodríguez, and R. R. Rodríguez-Guzmán, *J. Phys. G* **46**, 013001 (2019).
- [55] S. Goriely, S. Hilaire, M. Girod, and S. Péru, *Phys. Rev. Lett.* **102**, 242501 (2009).
- [56] K. Nomura, R. Rodríguez-Guzmán, and L. M. Robledo, *Phys. Rev. C* **94**, 044314 (2016).
- [57] J. Ginocchio and M. Kirson, *Nucl. Phys. A* **350**, 31 (1980).
- [58] K. Nomura, N. Shimizu, and T. Otsuka, *Phys. Rev. Lett.* **101**, 142501 (2008).
- [59] K. Nomura, N. Shimizu, and T. Otsuka, *Phys. Rev. C* **81**, 044307 (2010).
- [60] K. Nomura, N. Shimizu, D. Vretenar, T. Nikšić, and T. Otsuka, *Phys. Rev. Lett.* **108**, 132501 (2012).
- [61] P. Van Isacker and J.-Q. Chen, *Phys. Rev. C* **24**, 684 (1981).
- [62] K. Heyde, P. Van Isacker, M. Waroquier, and J. Moreau, *Phys. Rev. C* **29**, 1420 (1984).
- [63] D. J. Rowe and J. L. Wood, *Fundamentals of Nuclear Models* (World Scientific, 2010).
- [64] J. Meyer-Ter-Vehn, *Phys. Lett. B* **84**, 10 (1979).
- [65] K. Sümmerer, N. Kaffrell, and N. Trautmann, *Nucl. Phys. A* **308**, 1 (1978).
- [66] T. Kibédi and R. Spear, *At. Data Nucl. Data Tables* **89**, 77 (2005).
- [67] T. Kibédi, A. Garnsworthy, and J. Wood, *Prog. Part. Nucl. Phys.* **123**, 103930 (2022).
- [68] H. Watanabe, K. Yamaguchi, A. Odahara, T. Sumikama, S. Nishimura, K. Yoshinaga, Z. Li, Y. Miyashita, K. Sato, L. Próchniak, H. Baba, J. Berryman, N. Blasi, A. Bracco, F. Camera, J. Chiba, P. Doornenbal, S. Go, T. Hashimoto, S. Hayakawa *et al.*, *Phys. Lett. B* **704**, 270 (2011).
- [69] J. Snyder, W. Reviol, D. Sarantites, A. Afanasjev, R. Janssens, H. Abusara, M. Carpenter, X. Chen, C. Chiara, J. Greene, T. Lauritsen, E. McCutchan, D. Seweryniak, and S. Zhu, *Phys. Lett. B* **723**, 61 (2013).
- [70] R. F. Casten, *Nuclear Structure from a Simple Perspective* (Oxford University Press, Oxford, 2000).
- [71] V. Werner, N. Pietralla, P. von Brentano, R. F. Casten, and R. V. Jolos, *Phys. Rev. C* **61**, 021301(R) (2000).